ARTICLE

Check for updates

Seawater sulphate heritage governed early Late Miocene methane consumption in the long-lived Lake Pannon

Zhiyong Lin [1✉], Harald Strauss[2], Jörn Peckmann [1], Andrew P. Roberts [3], Yang Lu[4], Xiaoming Sun[5], Tingting Chen[5] & Mathias Harzhauser[6]

Sulphate deficiency makes lake environments a key source of atmospheric methane because sulphate-driven anaerobic oxidation of methane (SD-AOM) is hindered. Miocene to Pliocene Lake Pannon was the largest European lake, although the extent of its methane production remains unclear. When sulphate is available, SD-AOM occurs commonly in anoxic sediments and is recorded by authigenic iron sulphides. Here we identify abundant tubular pyrite and greigite aggregates from Lake Pannon sediments, which record brackish early lake conditions at ~11.3 Ma. The iron sulphides are morphologically similar to those reported elsewhere from methane seep and gas hydrate environments. Microscale sulphur isotope analysis and multiple sulphur isotope patterns of iron sulphides, and elevated sedimentary Ba/Al and Mo/Al ratios, are consistent with their derivation from SD-AOM under marine conditions. These results indicate substantial methane consumption in early Lake Pannon, and that sulphate was the dominant oxidant for AOM, which reduced the release of sedimentary methane to the atmosphere. SD-AOM signals archived by iron sulphides are valuable for evaluating methane consumption in lacustrine sediments.

[1] Institut für Geologie, Zentrum für Erdsystemforschung und Nachhaltigkeit, Universität Hamburg, Hamburg 20146, Germany. [2] Institut für Geologie und Paläontologie, Westfälische Wilhelms-Universität Münster, Münster 48149, Germany. [3] Research School of Earth Sciences, Australian National University, Canberra, ACT 2601, Australia. [4] Natural History Museum, University of Oslo, Oslo 0318, Norway. [5] School of Marine Sciences, Sun Yat-sen University, 510006 Guangzhou, China. [6] Geological-Paleontological Department, Natural History Museum Vienna, Vienna 1010, Austria. ✉email: zhiyong.lin@uni-hamburg.de

Methanogenesis in anoxic marine and lacustrine systems produces substantial amounts of methane (~370 Tg yr^{-1}) during organic matter fermentation[1–3]. Sulphate is available in high concentrations in modern seawater (28 mM). In methane-rich marine environments, most methane is consumed at the expense of sulphate through sulphate-driven anaerobic oxidation of methane (SD-AOM)[2,4], which greatly reduces seabed methane release. In contrast, lacustrine sedimentary environments (e.g., lakes) typically have low-sulphate concentrations[5] and, thus, represent the largest (~90%) natural atmospheric methane source[3]. This is because sulphate is the most dominant electron acceptor for AOM[6]. Although it has been suggested that AOM in low-sulphate freshwater environments is coupled to nitrate, manganese or iron reduction[7–9], methane consumption via these pathways is largely regarded as inconsequential[3]. Experimental evidence indicates that high SD-AOM rates can occur under low-sulphate levels, rendering possible high methane consumption even in low-sulphate lacustrine sediments[10,11]. Sulphate availability is, thus, a key factor that affects methane consumption in lacustrine sediments[10]. Methane-rich lacustrine environments are commonly located along coastlines, resulting in changes of sulphate availability caused by sea-level change that affect the mode and degree of methane consumption[12,13]. In marine environments, SD-AOM has been recognised frequently in the geological record from highly ^{13}C-depleted seep carbonates, for example, in the middle Palaeozoic ocean[14]. However, geological evidence for methane consumption from lacustrine environments is scarce[15], which limits reconstruction of ancient methane carbon cycling.

Lake Pannon was a long-lived, large lake on the southern margin of the European plate and was the largest European late Cenozoic non-marine biodiversity hotspot[16,17]. The lake formed after a glacio-eustatic sea-level drop at ~11.6 Ma (Fig. 1), which led to final disintegration of the central and southeastern European Parathethys Sea[17–19]. During its maximum extent between 10.5 and 10.0 Ma, it covered around 233,500 km^2, attaining more than half the size of the modern Black Sea with a greatest depth of around 1000 m[17]. Biota and sedimentary features indicate that Lake Pannon was initially brackish and that it freshened gradually following isolation from the Parathethys Sea[16,18,19]. Its marine heritage might have impacted lake water sulphate concentrations and methane-related carbon cycling during early-stage lake evolution. However, little is known about methane formation and consumption in the lake due to the scarcity of suitable geochemical data[20–22]. As an authigenic sulphide mineral, pyrite derived from SD-AOM commonly carries characteristic geochemical signatures[23–25], which can constrain the sediment biogeochemistry of Lake Pannon.

Recently, an up to 4-m-thick pelite unit containing abundant tubular pyrite aggregates was detected in three adjacent boreholes in the Vienna Basin (Fig. 1). These formed at ~11.3 Ma during early-stage Lake Pannon[26,27], when the lake surface area was smaller with large islands[18] (Fig. 1a). During this period, bottom waters in Lake Pannon were well oxygenated down to the storm wave base in coastal sublittoral regions[28]. Deeper sublittoral regions of Lake Pannon had low oxygenation, which was only interrupted on millennial scales by increased bottom water oxygenation, as indicated by rapid but short-lived dreissenid bivalve settlements[29]. The tubular pyrite structures have not been reported from the well-studied younger lake sediments[30,31], and likely record early lake-stage biogeochemical processes. We present geochemical, mineralogical, and magnetic evidence to assess
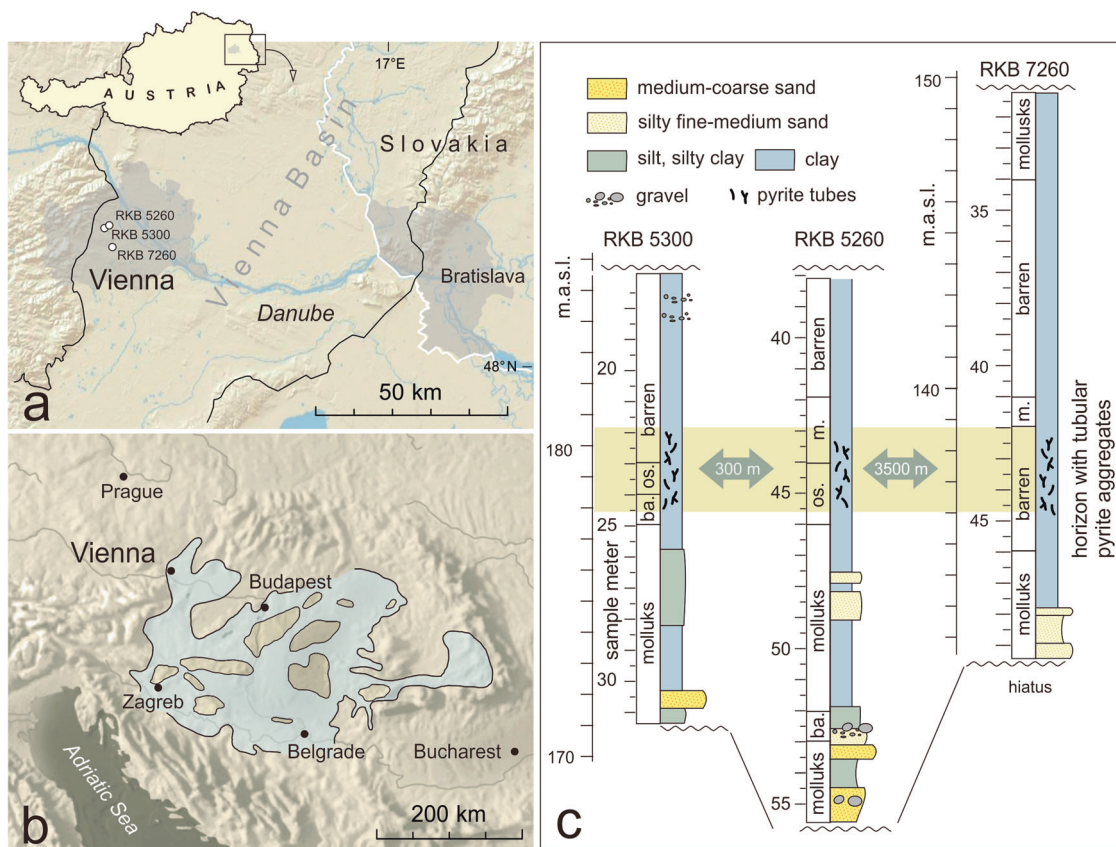
Fig. 1 Location of the study site and summary stratigraphy of the studied cores. a Position of the studied cores on the western margin of Vienna Basin; **b** Lake Pannon during the early Pannonian around 11.3 Ma[18]; **c** lithological logs of Pannonian lower PA1 parasequence from three drill cores; arrows indicate distances between drill sites[26]. ba. barren, m. molluscs, os. ostracods.

the origin of the pyrite aggregates and to test for SD-AOM signals to evaluate sulphur and carbon cycling in Lake Pannon.

Geological background and samples. The study area is located within the Vienna Basin, which is a rhombic extensional basin that strikes roughly SW-NE from Lower Austria in the SSW to the Czech Republic in the NNE (Fig. 1a). The Vienna Basin basement is formed by Alpine-Carpathian nappes, with Neogene basin fill that reaches a maximum thickness of 5500 m[32,33]. Three 60-m long cores, RKB 5260 (N 48.221543°, E 16.345415°), RKB 5300 (N 48.220493°, E 16.341733°) and RKB 7260 (N 48.196074°, E 16.352512°) (Fig. 1) were studied[27], which penetrated lower Pannonian lacustrine sediments (20.5–55.5 m in RKB 5260; 19.5–31.5 m in RKB 5300; and 9.5–60.0 m in RKB 7260, respectively). The cored sediments have uniform lithology and comprise clay and silty clay with a few intercalations of silty sand. Based on sedimentological, palaeontological, and geophysical data for these cores (Fig. 1c), two parasequences (Pannonian PA1 and PA2) were identified[26]. The lower PA1 parasequence formed in medium-deep sublittoral muddy lake bottom environments below the storm wave base during the first rapid transgression of Lake Pannon (Fig. 1b). Barren intervals indicate periods of severe bottom water anoxia at the boundary between the PA1 and PA2 parasequences, which were interrupted by short phases of biotic resettlement by Ostracoda and thin-shelled lymnocardiid bivalves[26]. Within lower parasequence PA1, a 3–4-m-thick interval contains abundant iron sulphide aggregates in the cores (RKB 5260: 46–43 m, RKB 5300: 25–22 m, RKB: 7260 45–41 m; Fig. 2). Pyrite tubes are accompanied by ostracod mass occurrences, with subordinate molluscs[26] (Fig. 1c). Based on the sedimentation rates[26], the 3–4-m-thick interval with tubular pyrite aggregates likely formed over ~4–6 kyr.

Results

**Mineralogy and morphology of pyrite and greigite aggregates**. To explore the nature of the iron sulphide aggregates, samples from core RKB 5260 were collected here for further analysis. Pyrite is the main phase in iron sulphide aggregates picked from sediment in core RKB 5260 (mainly from 43.0 to 47.2 m; Fig. 2 and Supplementary Figs. 1 and 2). Most aggregates are black and tubular, with similar habits and textures (Fig. 2a, b). The pyrite aggregates consist of clustered framboids with variable sizes (Figs. 2c and 3b). In many parts of the studied interval, framboidal pyrite aggregates are overgrown by secondary pyrite. These overgrowth layers fill the space between framboids (Fig. 2d, e). In some aggregates, oxidation products (e.g., goethite) occur as secondary layers around pyrite aggregates (Fig. 2f). Magnetic greigite aggregates occur mainly from 41.0 to 42.8 m in core RKB 5260. Most of the greigite occurs as black, irregular granular particles that commonly coexist with brownish goethite (Fig. 2g, h). Clusters of (i) fine greigite microcrystals and (ii) acicular crystals occur commonly within the aggregates (Fig. 2i, j). Greigite nanocrystals also occasionally coexist with pyrite framboids (Fig. 2k). X-ray diffraction analysis further indicates the occurrence of minor mackinawite in the greigite aggregates (Fig. 2).

Magnetic susceptibility (χ) and FORC diagrams. In core RKB 5260, higher χ values (up to $0.30 \times 10^{-6}\,\mathrm{m^3\,kg^{-1}}$) coincide with the presence of greigite aggregates (above 42.8 m), particularly from 41.0 to 41.6 m. In contrast, χ has low and constant values of $\sim 0.09\,\mathrm{m^3\,kg^{-1}}$ in intervals with pyrite aggregates (from 43.0 to 47.2 m). To characterise the magnetic domain state and magnetostatic interactions among magnetic particles, first-order reversal curves (FORCs)[34] were measured for bulk samples from intervals with different χ values (Fig. 3). FORC diagrams
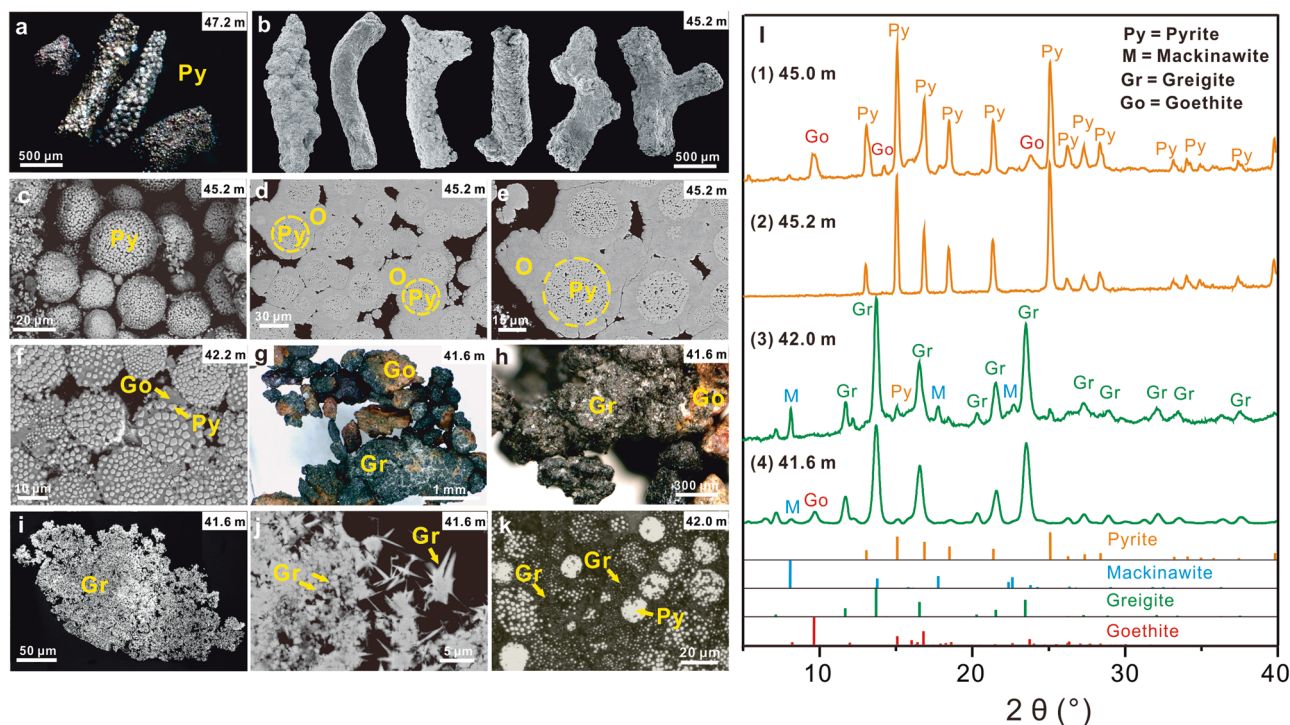
Fig. 2 Morphologies, structures, and mineralogical data for authigenic minerals. a, b Tubular pyrite aggregates. **c** Aggregate with pyrite framboids. **d, e** Resin-impregnated polished sections of pyrite framboids (Py) with overgrowths (O). **f** Goethite layer (Go) surrounding pyrite framboids. **g, h** Irregular granular greigite aggregates (Gr) and coexisting goethite. **i, j** Resin-impregnated polished sections of greigite aggregates. The large range of BSE intensities was caused by the occurrence of goethite. **k** Co-occurring framboidal pyrite and greigite nanocrystals. Fine particles are greigite and coarser/brighter particles are pyrite. (**a, g, h, k**) in optical microscope mode and (**b–f, i, j**) in SEM-BSE mode. **l** X-ray diffraction analyses of selected authigenic minerals from different depths.
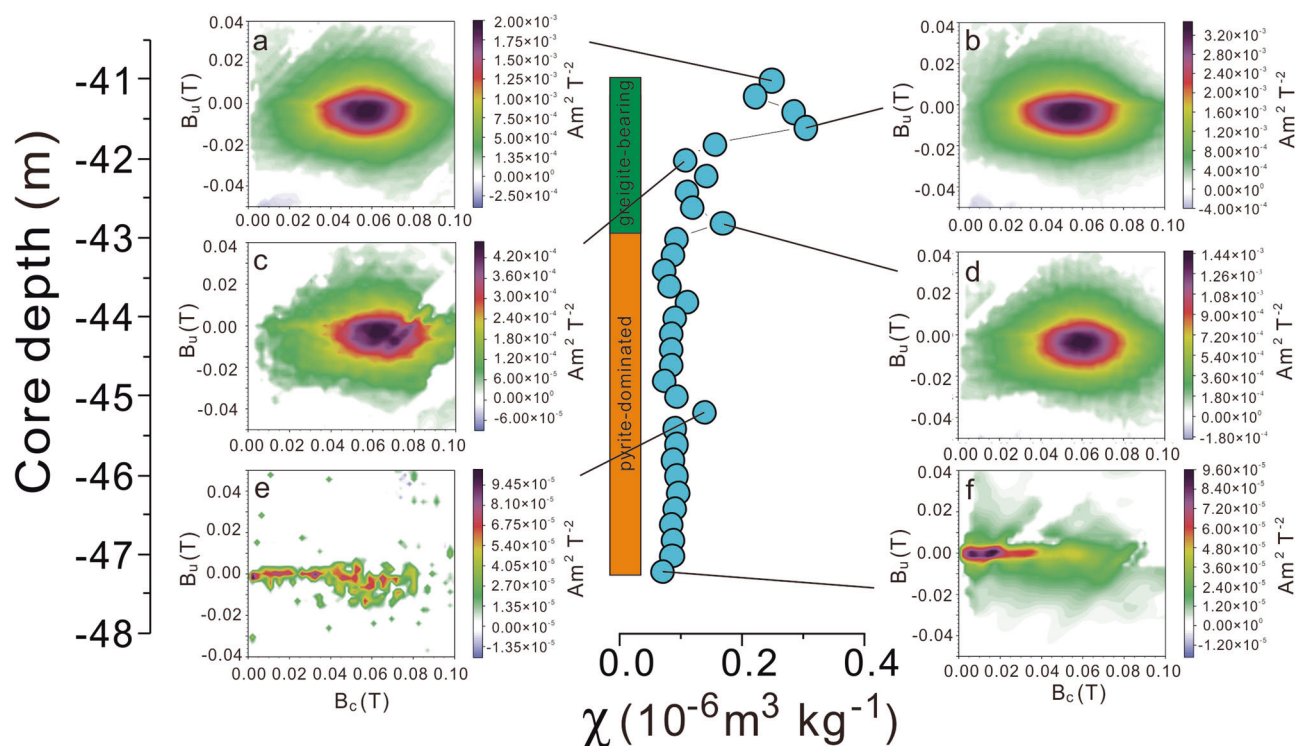
Fig. 3 First-order reversal curve (FORC) diagrams for typical bulk sediments from different depths in core RKB 5260. a–d Strongly magnetostatically interacting medium-coercivity single domain component, which is typical of greigite-bearing sediments from sulphidic and methanic diagenetic environments[36]. **e, f** Lower coercivity authigenic SP/SD greigite[35,36] in pyrite-dominated intervals. FORC diagrams were processed using the FORCsensei algorithm[88], which searches 1350 FORC models using all combinations of VARIFORC smoothing parameters[89] to produce optimal FORC distributions in which noise is smoothed without over-smoothing the underlying signal. VARIFORC parameters for each diagram are: **a** $s_{c,0} = 2$, $s_{c,1} = 2$, $s_{u,0} = 2$, $s_{u,1} = 2$, $\lambda = 0.00$, and $\psi = 0.64$; **b** $s_{c,0} = 2$, $s_{c,1} = 2$, $s_{u,0} = 2$, $s_{u,1} = 2$, $\lambda = 0.00$, and $\psi = 0.66$; **c** $s_{c,0} = 2$, $s_{c,1} = 2$, $s_{u,0} = 2$, $s_{u,1} = 2$, $\lambda = 0.04$, and $\psi = 0.51$; **d** $s_{c,0} = 2$, $s_{c,1} = 2$, $s_{u,0} = 2$, $s_{u,1} = 2$, $\lambda = 0.00$, and $\psi = 0.61$; **e** $s_{c,0} = 2$, $s_{c,1} = 2$, $s_{u,0} = 2$, $s_{u,1} = 2$, $\lambda = 0.00$, and $\psi = 0.54$; **f** $s_{c,0} = 3$, $s_{c,1} = 5$, $s_{u,0} = 3$, $s_{u,1} = 5$, $\lambda = 0.16$, and $\psi = 0.57$.

are similar for greigite-bearing sediments with high χ values ($>0.10 \times 10^{-6}\,\mathrm{m^3\,kg^{-1}}$; Fig. 3). They reveal a magnetostatically interacting stable SD greigite component with high coercivity (Fig. 3a–d), which is typical of greigite-bearing sediments from sulphidic and methanic diagenetic environments[35,36] and are consistent with the presence of greigite aggregates. In pyrite-dominated intervals with low χ values, the FORC diagrams (Fig. 3e, f) indicate the presence of lower contents of authigenic SP/SD greigite with lower coercivity[35,36].

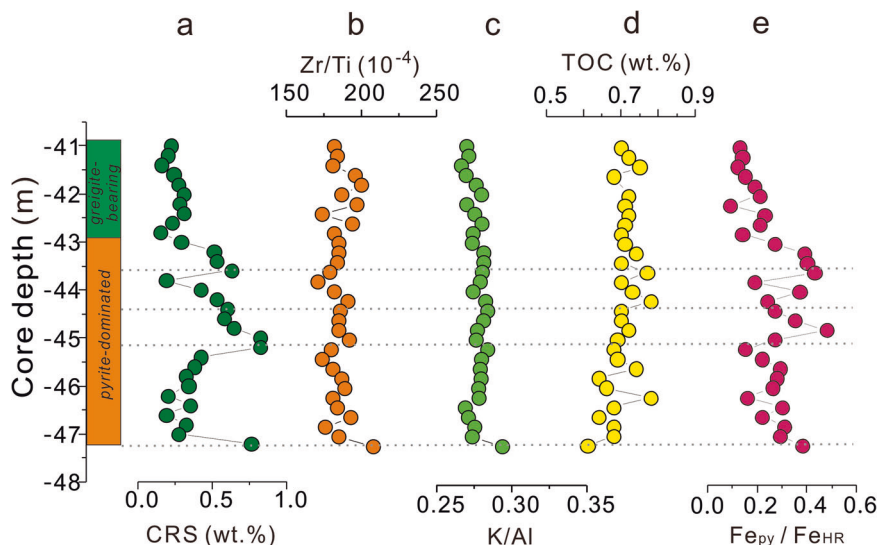**Chromium reducible sulphur (CRS) content and iron speciation.** Total CRS contents in core RKB 5260 are generally low (<0.25 wt.%) except for four distinct peaks at 43.6 m, 44.4 m, 45.2 m and 47.2 m (Fig. 4). Among the three non-sulphur-bound reactive iron components ($Fe_{acetate}$, $Fe_{dithionite}$, $Fe_{oxalate}$), $Fe_{acetate}$ is the main iron pool in all samples. These iron components have similar trends despite variable contents, with distinctive peaks at depths of 42.2 m, 44.4 m, 45.2 m and 47.2 m (Fig. 5). Assuming that CRS is derived totally from pyrite (1:2 stoichiometry of Fe:S), pyrite-bound iron (Fe_{py}) is obtained from the CRS content of each sample. The total reactive iron (Fe_{HR}) is the sum of $Fe_{acetate}$, $Fe_{dithionite}$, $Fe_{oxalate}$ and Fe_{py}. The extent of pyritization (Fe_{py}/Fe_{HR} ratio) is typically lower than 0.4 throughout the studied interval (Fig. 5).

Sulphur isotopic compositions. Within greigite-bearing sediments (i.e., 41.0–42.8 m, core RKB 5260), $\delta^{34}S_{CRS}$ values are relatively constant at +3.5‰ ($n = 10$) (Fig. 6). Corresponding $\Delta^{33}S_{CRS}$ values vary over a narrow range close to 0‰ (Fig. 7).

From 43.0 to 47.2 m, the multiple sulphur isotope compositions of CRS (pyrite) are characterised by large $\delta^{34}S_{CRS}$ (from −15.2 to +7.4‰) and $\Delta^{33}S_{CRS}$ variations (−0.04 to +0.03‰, $n = 22$) (Fig. 7). $\delta^{34}S_{pyrite}$ values of hand-picked pyrite aggregates range from −11.7 to +8.6‰ (Fig. 6).

Two pyrite varieties—framboids and overgrowth layers—from various depths were targeted for SIMS analysis (Fig. 6). However, complex composite pyrite aggregate textures proved difficult to resolve even for SIMS analysis with 15-μm spot size. To avoid mixed signals from different paragenetic phases during analysis, only larger pyrite aggregates (>20 μm) were measured (Supplementary Figs. 3 and 4). In some cases, possible admixture between overgrowths and framboids cannot be excluded[24]; such slightly mixed spot analyses are classified here as pyrite overgrowths (Supplementary Figs. 3 and 4).

$\delta^{34}S_{SIMS}$ values for the two pyrite varieties are highly variable for each pyrite aggregate from the same depth and through the studied interval (Fig. 6). A total spread of 106‰ was obtained for pyrite $\delta^{34}S_{SIMS}$ values, ranging from −58.7 to +45.3‰ (Fig. 6). Larger pyrite framboids and extensive pyrite overgrowths are abundant in pyrite-dominated intervals (from 43.0 to 47.2 m). In these intervals, $\delta^{34}S_{SIMS}$ values of intimate pyrite overgrowth layers tend to be higher than for early pyrite framboids. The $\delta^{34}S_{SIMS}$ difference between framboids and overgrowths can be up to 30‰ in a single aggregate. Only a few pyrite aggregates were chosen for sulphur isotope measurements from each sample; therefore, the obtained $\delta^{34}S_{SIMS}$ values might not reflect the entire variability of $\delta^{34}S_{SIMS}$ values. This circumstance explains some mismatches between $\delta^{34}S_{CRS}$ and $\delta^{34}S_{SIMS}$ values.

Fig. 4 Geochemical data for core RKB 5260. a Chromium reducible sulphur (CRS) content. **b** Zr/Ti and **c** Zr/Ti ratios. **d** Organic matter content. **e** Extent of pyritization (Fe$_{py}$/Fe$_{HR}$ ratio; Fe$_{HR}$ = Fe$_{acetate}$ + Fe$_{dithionite}$ + Fe$_{oxalate}$ + Fe$_{py}$).
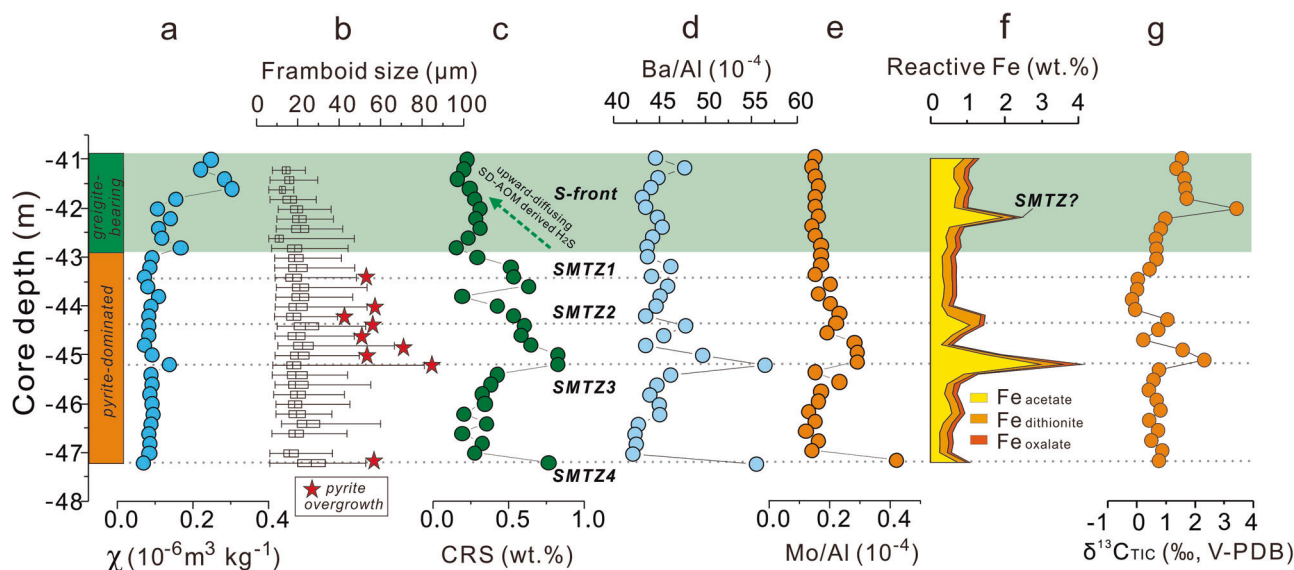

Fig. 5 Magnetic susceptibility, framboid size distribution and geochemical data for core RKB 5260. a Mass magnetic susceptibility of bulk sediment. **b** Framboid size distributions in box-and-whisker plots, where boxes extend from quartile $Q = 0.25$ to 0.75 and include 50% of data. The vertical line in the box is the median; lines at the left- and right-hand sides are minimum ($Q = 0.00$) and maximum ($Q = 1.00$) values. **c** Chromium reducible sulphur (CRS) content. **d** Ba/Al and **e** Mo/Al ratios. **f** Iron species distribution in the sediment. **g** δ^{13}C of total inorganic carbon in bulk sediments. The shaded zone refers to greigite-dominated sediments.

Trace element contents of bulk sediments. Zr/Ti, K/Al, Ba/Al, Mo/Al and P/Al ratios are shown in Figs. 4 and 5. Zr/Ti and K/Al ratios are constant through the studied horizons corresponding to around 185 (*10^{-4}) and 0.28, respectively. In contrast, Ba/Al, Mo/Al and P/Al ratios vary with peaks in some CRS rich layers (e.g., 45.6 and 47.2 m).

Total inorganic carbon contents and carbon isotopic compositions. Throughout the studied stratigraphic interval, sedimentary total inorganic carbonate (TIC) has low contents of 1.3–2.8 wt.%. δ^{13}C$_{TIC}$ values for bulk sediments range from -0.2 to $+3.4‰$ ($n = 32$; Fig. 5), with some peaks coinciding with layers enriched in Fe$_{acetate}$.

Discussion

Evidence for SD-AOM in Lake Pannon sediments. Sedimentary pyrite formation is impacted by sulphate reduction processes such as organoclastic sulphate reduction (OSR)[37] and sulphate-driven anaerobic oxidation of methane (SD-AOM), and by the availability of reactive iron compounds[38,39]. Pyrite formation is thought to be controlled either by (i) the polysulphide pathway[40] or (ii) the hydrogen sulphide pathway[41]. For both pathways, aqueous iron (II) monosulphide or surface-bound species on minerals like mackinawite can react with dissolved sulphide or polysulphide to promote pyrite formation (see Rickard[39] for a review). It has also been suggested that pyrite can form directly under Fe(II)-excess conditions, such as in sedimentary environments with abundant ferric (oxyhydr)oxides[42].
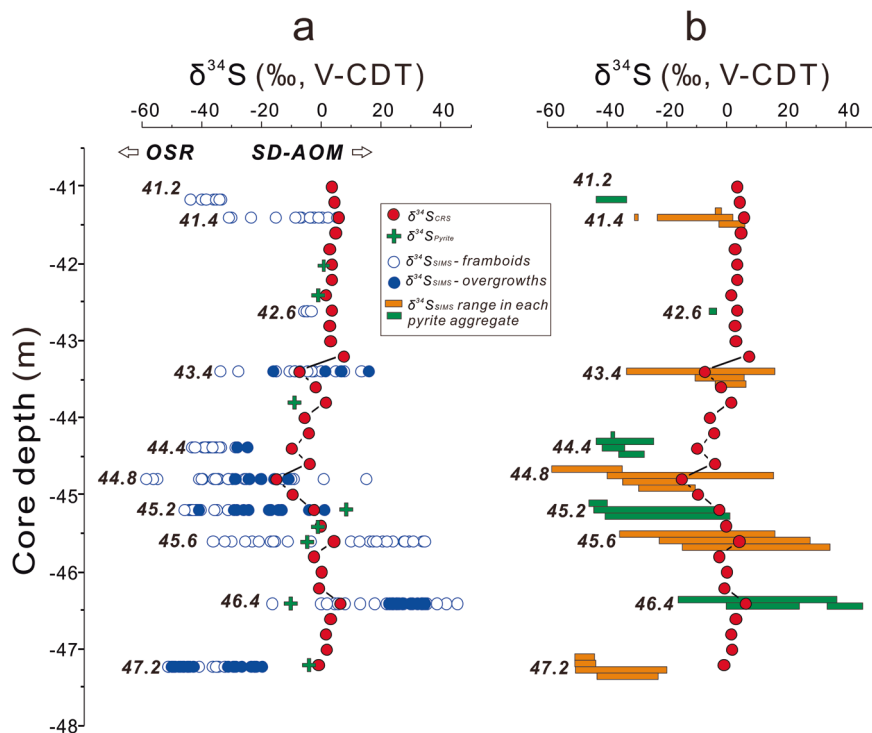
Fig. 6 Sulphur isotope data for core RKB 5260. a Sulphur isotopic composition of CRS ($\delta^{34}S_{CRS}$) and hand-picked pyrite tubes ($\delta^{34}S_{Pyrite}$) in bulk sediments and in-situ pyrite SIMS $\delta^{34}S_{SIMS}$. **b** Distribution pattern of $\delta^{34}S_{SIMS}$ variation of each pyrite aggregate from different depths.
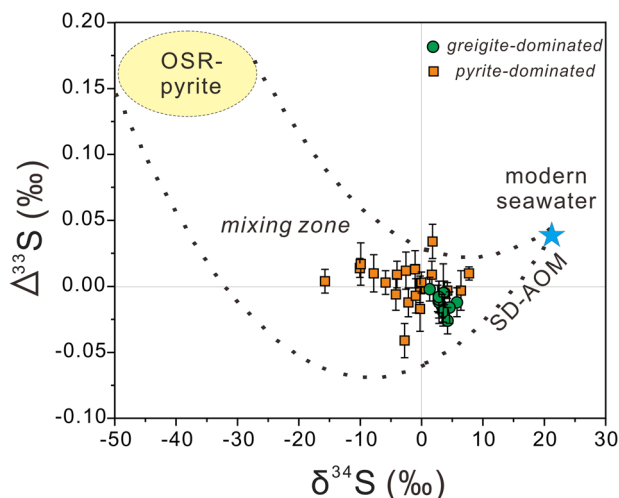
Fig. 7 Variation of $\delta^{34}S$ and $\Delta^{33}S$ values for chromium reducible sulphur (CRS) in pyrite- and greigite-dominated depths from core RKB 5260. The yellow oval (labelled 'OSR-pyrite') represents typical sulphur isotope compositions of pyrite derived from organoclastic sulphate reduction (OSR) in shallow sediments of modern marine seep environments[45,49]. All data for pyrite-dominated (orange squares; 43.0–47.2 m) and greigite-dominated samples (green circles; 41.0–42.8 m) align along the mixing zone between OSR-pyrite and modern seawater sulphate end members. Error bars are from standard deviation (SD) for $\Delta^{33}S$ values.

The degree of pyritization (Fe_{py}/Fe_{HR}) throughout the studied interval ranges mainly from 0.1 to 0.5, which is below the threshold (0.8) for euxinic conditions[43]. This indicates that reactive iron is abundant throughout the studied interval. Therefore, pyrite enrichment in multiple horizons was unlikely to be controlled by reactive iron availability under sulphidic conditions. Moreover, pyrite tubes are accompanied by massive

ostracod occurrences[26] (Fig. 1c), which suggest oxic water column conditions. Input of detritus was constant (indicated by Zr/Ti and K/Al)[44] and organic matter contents do not vary much (41.0–47.2 m; Fig. 4). This cumulative evidence argues against a mode of pyrite formation that reflects changes of water geochemistry resulting from either a change of detrital input or productivity.

Pyrite aggregates in the studied sediments mostly have tubular shapes (Fig. 2) with late-stage overgrowths, which is reminiscent of aggregates forming in modern methane seeps and gas-hydrate environments[24,45–47]. The tubular shape likely represents sedimentary micro-channels created by pressurised advection or diffusion of methane-rich fluids[24]. The tubular void spaces were later filled by pyrite. Intervals with high pyrite contents (Fig. 4a), therefore, likely result from enhanced SD-AOM and point to the positions of palaeo-sulphate methane transition zones (palaeo-SMTZs)[24,45]. Extensive overgrowths on framboids suggest that SD-AOM led to fluids supersaturated in dissolved sulphide, which favoured pyrite framboid and overgrowth formation[24,39].

Throughout the studied interval (41.0–47.2 m, core RKB 5260), framboids commonly have low $\delta^{34}S_{SIMS}$ values (as low as −59‰; Fig. 6). This points to OSR with preferential microbial ^{32}S-sulphate uptake[24,45,48,49]. In contrast, higher bulk sediment $\delta^{34}S_{CRS}$ (from −15.2 to +7.4‰) suggests admixture of ^{34}S-enriched pyrite, probably derived from SD-AOM[24,45,46,50]. Considering the presence of two pyrite end members derived from OSR and SD-AOM, the pyrite sulphur isotopic compositions should represent mixing between these end members[45,46,49]. Pore water sulphate is thought to be converted quantitatively to sulphide within the SMTZ during SD-AOM[51], with isotope mass balance resulting in the $\delta^{34}S$ values of hydrogen sulphide leaning toward the original isotopic composition of dissolved sulphate[50]. All analysed pyrite samples have intermediate values between those of OSR-derived pyrite and modern seawater sulphate (Fig. 7). Thus, pyrite derived from SD-AOM in Lake Pannon

likely reflects an aggregated sulphate sulphur isotopic composition similar to that of modern seawater sulphate ($\delta^{34}S = +21.24‰$ and $\Delta^{33}S = +0.050‰$)[52]. This mixing scenario is also supported by the multiple sulphur isotope pattern obtained by SIMS analysis (Supplementary Fig. 5). Lake Pannon pyrite has extremely wide-ranging $\delta^{34}S_{SIMS}$ values (Fig. 6). Pyrite $\delta^{34}S_{SIMS}$ commonly increases from framboids to overgrowth layers within the same aggregate. For example, for the 43.4 m and 45.2 m intervals, the wide range of pyrite $\delta^{34}S_{SIMS}$ values indicates continuous and finally near-complete dissolved sulphate consumption near the SMTZ following Rayleigh-type distillation[24,45]. However, pyrite derived from SD-AOM can also have low $\delta^{34}S$ due to enhanced diffusive sulphate replenishment derived from seawater or oxidative sulphur cycling[53]. Authigenic ^{13}C-depleted seep carbonates record SD-AOM[54] and can co-occur with ^{34}S-enriched pyrite at SMTZs[49,55]; yet no $^{13}C_{TIC}$ depletion is observed at the identified palaeo-SMTZs in Lake Pannon. Such absence of ^{13}C-depleted carbonate is common at the SMTZ[24,56,57], and is a function of the local sedimentary environment (e.g., pH). Methanogenesis typically occurs below the SMTZ and results in higher $\delta^{13}C$ values of dissolved bicarbonate. Therefore, positive $\delta^{13}C_{TIC}$ values likely reflect upward diffusion of dissolved inorganic carbon from methanogenesis below the SMTZ[58]. In addition to high $\delta^{13}C_{TIC}$ values, the same horizons with relatively high $\delta^{13}C_{TIC}$ values have elevated $Fe_{acetate}$ contents (Fig. 5), which suggest Fe(II)-rich environments. These patterns are consistent with upward diffusion of Fe(II) derived from iron reduction in the methanic zone[7,59]. Finally, given the succession of biogeochemical processes in space and time and the presence of steep geochemical gradients in sedimentary environments where methane is present, some of the observed geochemical signatures are likely to reflect mixed signals observed in the same horizon.

Greigite is a metastable ferrimagnetic iron sulphide mineral that is common in lake sediments and is considered to record lake geochemistry[60–62]. Greigite is also present in marine sediments and has been reported widely from methane seeps and gas-hydrate-bearing environments[63–66]. Greigite occurrences can represent sulphidization fronts around the SMTZ, where it transforms into pyrite upon supply of excess hydrogen sulphide[63,65]. In the Lake Pannon sediments, greigite tends to occur in horizons with limited pyrite (i.e., above 43.0 m). In a $\Delta^{33}S/\delta^{34}S$ plot, all greigite-dominated samples have more negative $\Delta^{33}S$ values than expected for OSR-derived sulphide forming in a seawater sulphate-dominated environment (quadrant II). Values for greigite are closer to those for seawater sulphate (Fig. 7) and are more consistent with the pattern for iron sulphides derived from SD-AOM[45,49,53,67]. In contrast to the wide range of $\delta^{34}S_{CRS}$ values for pyrite-dominated depths, $\delta^{34}S_{CRS}$ values from greigite-dominated sediments fall within a narrow range (Fig. 7), which suggests that greigite formation was rapid and associated with hydrogen sulphide diffusion from the SMTZ. FORC diagrams for sediments from greigite-bearing intervals (Fig. 3) are typical of authigenic greigite from methane-rich sedimentary environments[36], which is consistent with an origin from SD-AOM.

Variable redox conditions controlled by seepage dynamics. In modern marine seep environments, spatiotemporal methane flux variations commonly lead to vertical SMTZ movement, as evident from sedimentary geochemical signatures[49,68]. Elevated Mo/Al ratios occur at some of the inferred palaeo-SMTZs of early Lake Pannon sediments (e.g., 47.2 m; Fig. 5e). Along modern continental margins, dissolved Mo in pore water is mainly derived from seawater and commonly decreases with depth due to

scavenging by authigenic iron sulphide formation in the sediment. Thus, Mo enrichment at methane seeps typically reflects enhanced Mo fixation in authigenic iron sulphides at shallow SMTZs[25,68,69]. Therefore, pyrite-independent Mo/Al ratios of the background sediment at the inferred SMTZs suggests changes in the depth of the SMTZ, probably controlled by methane flux. Likewise, Ba/Al peaks at some SMTZs of today's marine sediments imply authigenic barite formation just above the SMTZ, which is also impacted by SMTZ mobility[70]. Overall, in addition to the presence of tubular pyrite aggregates and greigite formation, evidence for multiple palaeo-SMTZs (Fig. 5) suggests the former prominent presence of methane seepage in Lake Pannon. Although mechanisms controlling methane flux at ~11.3 Ma are not well-defined, it is likely that the low lake water level (~200 m depth; Harzhauser et al., unpublished seismic data) triggered a methane seepage increase in the lake[71].

Within the SMTZ, hydrogen sulphide released from SD-AOM commonly leads to sulphidic dissolution of reactive iron[72]. Thus, iron (oxyhydr)oxide contents and magnetisation can be markedly reduced at the SMTZ[35,72]. However, we find no such reactive iron decrease (e.g., $Fe_{acetate}$, $Fe_{dithionite}$, $Fe_{oxalate}$) at the inferred palaeo-SMTZs (SMTZ1-4; Fig. 5). Na-acetate solution can extract substantial Fe(III) from amorphous iron (oxyhydr)oxides[73,74], where $Fe_{acetate}$ is from iron carbonates and poorly crystalline Fe(III) minerals, whereas $Fe_{dithionite}$ and $Fe_{oxalate}$ include crystalline haematite, goethite, or magnetite[73,75]. High reactive iron contents at the inferred palaeo-SMTZs can, therefore, be caused by iron sulphide oxidation after burial. However, this fails to explain low reactive iron contents at SMTZ1 (i.e., 43.4 m) where pyrite is abundant (Fig. 5). Alternatively, vertical SMTZ movement at dynamic seep sites and resultant changing redox conditions could have caused iron sulphide oxidation within a former SMTZ and secondary iron (oxyhydr)oxide formation[76].

We propose the following scenario to explain the increased reactive iron content at three palaeo-SMTZs (Fig. 8). Sulphide formation during SD-AOM caused iron sulphide accumulation at or near a shallow SMTZ when methane fluxes were high, which was possibly caused by reduced hydrostatic pressure during lake-level lowstands. When seepage diminished, downward moving, seawater-derived fluids promoted iron sulphide oxidation at the former SMTZ, and secondary iron (oxyhydr)oxide formed[76]. Remaining iron sulphide would maintain the primary $\delta^{34}S$ patterns because sulphur isotope effects for the involved oxidative processes are small[77]. Resurgent high methane fluxes and positioning of the new SMTZ at shallower depths, possibly in combination with rapid burial, subsequently promoted iron (oxyhydr)oxide preservation without further alteration by sulphidization[76].

Sulphate-rich water in Lake Pannon. In marine sulphate-rich environments, most upward-diffusing methane is consumed at the expense of sulphate during SD-AOM[2]. Although low-sulphate freshwater environments might have high AOM rates[10], sulphur-bearing mineral formation (e.g., pyrite, gypsum) is limited in lake deposits. Multiple horizons with abundant tubular pyrite, as documented here, have also been observed in modern marine methane seep areas[49]. Sulphur isotopic compositions of pyrite at palaeo-SMTZs from Lake Pannon resemble observations from authigenic, SD-AOM-derived pyrite in modern seep environments, where seawater sulphate is the main sulphur source for pyrite formation[45,46,49]. It is, thus, likely that lake water sulphate in Lake Pannon had a similar sulphur isotopic composition as contemporary seawater sulphate. Although the initial sulphate concentration remains unknown, abundant tubular pyrite derived from enhanced SD-AOM indicates that dissolved sulphate was a
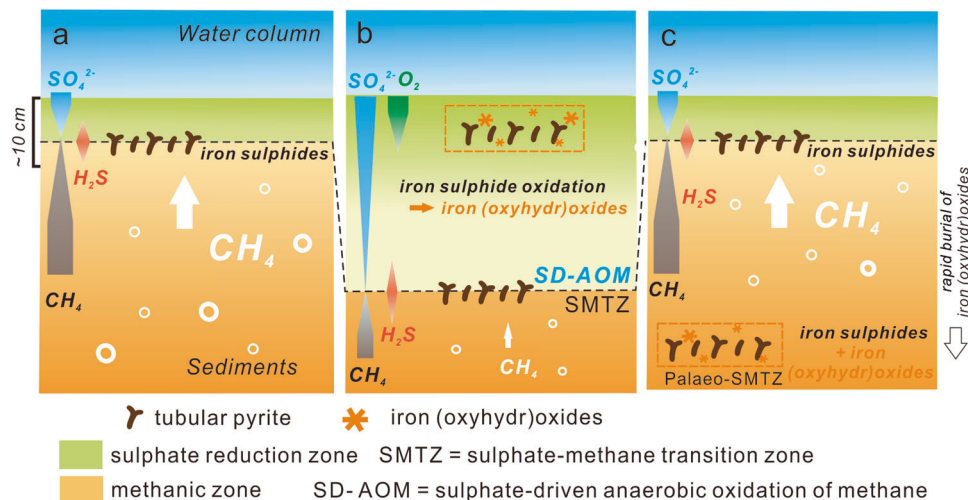
Fig. 8 Simplified scenario for dynamic sulphur and iron cycling in sediments under the influence of variable seepage intensities. a During high seepage activity, the sulphate methane transition zone (SMTZ) is located near the sediment surface. Within the SMTZ, sulphate-driven anaerobic oxidation of methane (SD-AOM) results in hydrogen sulphide release and pyrite formation. Upward- and downward-diffusing hydrogen sulphide leads to greigite formation. **b** After a decline of seepage intensity, downward moving oxidising fluids promote iron sulphide oxidation at the former SMTZ, which leads to secondary iron (oxyhydr)oxide formation. **c** Resurgence of high methane flux and/or rapid sediment burial promote iron (oxyhydr)oxide preservation during burial into a methanic environment without further alteration by sulphidization.

major lake water anion. Therefore, AOM coupled to nitrate, iron, and manganese reduction can be excluded as main pathways for methane consumption[7–9]. Tubular pyrite aggregates have been reported only from lower Pannonian deposits and not from the well-studied younger Pannonian sediments. This suggests that Lake Pannon initially had a marine sulphate signature, reflecting its Central Paratethys Sea heritage. Likewise, during isolation of Lake Pannon from the Paratethys Sea[16,18,19], Vienna Basin sediment could still have contained sufficient organic matter for methane production at depth. The still high sulphate pool and enhanced methane flow would have, thus, stimulated SD-AOM and enhanced sedimentary methane consumption. Subsequent lake freshening led to a dissolved sulphate decrease in the water column. Although SD-AOM can also occur at lower sulphate levels, pyrite formation and preservation might be impeded by the reduced dissolved sulphate concentration. We, therefore, make a case for use of authigenic pyrite to constrain carbon cycling in methane-rich environments and to assess its effects on climate.

Conclusions. Distinct horizons with abundant tubular iron sulphide aggregates are reported here from upper Miocene deposits of the early stage of the ancient European mega-lake, Lake Pannon. Geochemical, mineralogical, and magnetic analyses indicate that sedimentary iron sulphide formation resulted largely from SD-AOM.

(i) Multiple sediment layers from early-phase Lake Pannon with high pyrite contents represent palaeo-SMTZs, as supported by multiple proxies (e.g., Ba/Al, Mo/Al). $\delta^{34}S_{SIMS}$ values of pyrite are highly variable (-58.7 to $+45.3‰$; $n = 223$), and pyrite overgrowths on framboids typically have higher $\delta^{34}S_{SIMS}$ values than framboids. Sulphur isotopic compositions of bulk pyrite range from -15.2 to $+7.4‰$ for $\delta^{34}S_{SIMS}$, and from -0.04 to $+0.03‰$ for $\Delta^{33}S$, which represent signatures of the combined effects of OSR and SD-AOM.

(ii) Sulphur isotopic compositions of bulk greigite range from $+1.3$ to $+5.8‰$ for $\delta^{34}S_{CRS}$, and from -0.03 to $0‰$ for $\Delta^{33}S_{CRS}$. These narrow ranges suggest rapid greigite formation, likely caused by hydrogen sulphide diffusion

from SMTZs. FORC diagrams for authigenic greigite-bearing samples are consistent with those reported from marine methane seeps and gas-hydrate-bearing environments.

(iii) Iron (oxyhydr)oxides are found to be enriched in palaeo-SMTZs, along with abundant iron sulphides. The former are interpreted to have resulted from iron sulphide oxidation at shallow depths at times when methane flux was reduced.

Our data are consistent with intensified methane consumption at the expense of sulphate in early Lake Pannon. Although precise sulphate levels during early lake stages are unknown, its marine Paratethyan heritage favoured SD-AOM as a key biogeochemical process that governed carbon cycling in the methane-rich sediments of Lake Pannon.

Methods

Sediment samples from a 6-m-thick interval of core RKB 5260 (41.0–47.2 m) were collected at 20-cm intervals for this study. Sediment aliquots were treated with diluted hydrogen peroxide for several hours and were then washed with tap water and sieved through a set of standard sieves. Authigenic black iron sulphide aggregates (pyrite and greigite) were hand-picked from the coarse fraction under a binocular microscope. Greigite-bearing aggregates were extracted with a rare earth hand-magnet. For petrographic observations, representative iron sulphide aggregates were examined with a ΣIGMA field emission SEM after carbon coating at the School of Earth Science and Engineering, Sun Yat-Sen University, China.

Mineral composition identification was performed at the Norwegian Center for Mineralogy, Oslo. Mineral compositions were analysed via micro-XRD after morphological observations. Targeted particles were scraped from epoxy-mounted samples with a knife or were picked from sediments. Targeted ~100 μm particles were picked for morphological observations. Samples were attached to a fibre loop stage and aligned with the X-ray beam of a Rigaku XtaLAB Synergy-S single-crystal X-ray diffractometer (Mo Kα). X-ray diffraction patterns were measured by Gandolfi move mode for powders at 50 kV and 1 mA. The detector distance was 65 mm and the exposure time was 30 s for each detector theta position. Major phases were identified with the Bruker DIFFRAC.EVA software.

Magnetic measurements were performed on freeze-dried bulk sediment at the School of Earth Sciences and Engineering, Sun Yat-Sen University. Sediment magnetic susceptibility (χ) was measured at 976 Hz in a 200 Am^{-1} field with an AGICO MFK1-FA Kappabridge system. First-order reversal curve (FORC) diagrams were measured at 0.2 mT field steps with 0.5 s averaging time.

Sulphide sulphur from bulk sediment was liberated as hydrogen sulphide via wet chemical sequential extraction[78,79]. Acid-volatile (mono)sulphides (AVS) were liberated with HCl (25%) for 1 h at room temperature, but no AVS was detected

during extraction. The remaining samples were reacted with 1 M $CrCl_2$ solution at sub-boiling temperatures for 2 h in an inert nitrogen atmosphere to liberate CRS pyrite, including greigite. Released hydrogen sulphide from CRS was precipitated as zinc sulphide using a 3% acetic acid zinc acetate solution. Zinc sulphide precipitates were subsequently converted to silver sulphide (Ag_2S) using a 0.1 M $AgNO_3$ solution. Ag_2S precipitates were collected by filtration (<0.45 μm) and dried at 40 °C overnight. The CRS content was determined gravimetrically based on the Ag_2S yield.

For $\delta^{34}S$ analysis, Ag_2S precipitates were measured as SO_2 via combustion of a ~ 200 μg sample mixed with an equal amount of V_2O_5 using a ThermoScientific Delta V mass spectrometer linked to an Elemental Analyzer (EA-IRMS) at the Institut für Geologie und Paläontologie, Westfälische Wilhelms-Universität Münster. The isotope ratio is expressed in relation to the Vienna Canyon Diablo Troilite (V-CDT) standard with analytical precision better than ±0.3‰:

$$\delta^{34}S\,(‰,\,V-CDT) = \left[\left(\frac{(^{34}S/^{32}S)_{sample}}{(^{34}S/^{32}S)_{V-CDT}}\right) - 1\right] \times 1000$$

$\delta^{34}S$ measurements were calibrated with international reference materials IAEA-S1 ($\delta^{34}S = -0.30‰$), IAEA-S2 ($\delta^{34}S = 22.62‰$), IAEA-S3 ($\delta^{34}S = -32.49$) and NBS 127 ($\delta^{34}S = 20.3‰$)[80].

For multiple sulphur isotope measurements (i.e., ^{32}S, ^{33}S, ^{34}S, and ^{36}S), ~2.5 mg of Ag_2S was fluorinated to sulphur hexafluoride (SF_6) by reaction with 5 times excess of F_2 at 300 °C for 8 h in nickel reactors[81]. Following cryogenic and gas chromatographic purification, the multiple sulphur isotopes were measured using a ThermoScientific MAT 253 mass spectrometer at the Institut für Geologie und Paläontologie, Westfälische Wilhelms-Universität Münster. Results are calculated from $\delta^{33}S$, $\delta^{34}S$ and $\delta^{36}S$ and expressed as $\Delta^{33}S$ values[82]:

$$\Delta^{33}S\,(‰) = \delta^{33}S - 1000 \times \left[\left(1 + \frac{\delta^{34}S}{1000}\right)^{0.515} - 1\right]$$

The multiple sulphur isotope measurements were calibrated with international reference material IAEA-S1 ($\delta^{34}S = -0.30‰$ and $\delta^{33}S = -0.055‰$)[81]. Analytical precision is better than ±0.02‰ (2 SD) for $\Delta^{33}S$.

For SIMS analysis, selected pyrite and greigite samples were mounted on epoxy discs (25 mm diameter). The pyrite tubes were then cut, ground, and polished. SIMS analyses were made with a Cameca IMS1280-HR at the Guangzhou Institute of Geochemistry, Chinese Academy of Sciences[83]. A primary Cs^+ ion beam (~2.0 nA current, 20 kV total impact energy) was focused at the sample surface with a 15-μm spot diameter. A 15-μm raster was applied during all analyses to slightly homogenise the Gaussian beam. Pre-sputtering for 20 s was applied to remove the Au coating, and a normal-incidence electron gun was used for charge compensation. The mass resolving power was set at ~5000 to avoid isobaric interference. A NMR field sensor was used to stabilise the magnetic field. ^{32}S, ^{33}S and ^{34}S were measured simultaneously by three Faraday cups in the multi-collector system (L'2, L1 and H1, respectively). The total analysis time for each spot was ~4 minutes. An off-mount calibration procedure was used[83]. Pyrite standard UWPy-1 ($\delta^{34}S = 16.04 \pm 0.18‰$)[84] was used as the primary standard, and PPP-1 ($\delta^{34}S = 5.3 \pm 0.20‰$)[85] was used as a quality control standard. Pyrrhotite standard YP-136 ($\delta^{34}S = 1.5 \pm 0.1‰$)[83] was mounted together with the studied pyrite aggregates in epoxy discs to monitor analytical reliability. Standard YP-136 was measured at regular intervals between the analysis of every five samples. The isotope ratio is expressed as $\delta^{34}S$ with the V-CDT standard. Analytical precision is better than ±0.2‰ for $\delta^{34}S$.

Sequential extraction of solid-phase sedimentary iron pools by different solutions was carried out following the procedure of Poulton and Canfield[75] to quantify the following three iron mineral pools: (1) Na-acetate solution extracted iron ($Fe_{acetate}$): extracted using 10 ml of 1 M Na-acetate solution for 24 h, at solution pH 4.5 and ultrasonic vibration (UV) at 50 °C; (2) dithionite solution extracted iron ($Fe_{dithionite}$): 10 ml of 50 g l^{-1} Na dithionite and 0.2 mol l^{-1} tri-Na citrate, pH 4.8, with 2 h UV at room temperature; (3) oxalate solution extracted iron ($Fe_{oxalate}$): 10 ml of 0.2 mol l^{-1} ammonium oxalate and 0.17 mol l^{-1} oxalic acid, with 6 h at room temperature. Between each extraction step, residues were washed with 10 ml deionized water twice. Leachates from the above three steps were measured by solution inductively coupled plasma–atomic emission spectrometry (ICP-AES). Analytical reproducibility was typically better than ±5% (2 SD). Assuming that all CRS is from pyrite (1:2 stoichiometry of Fe/S), pyrite-bound iron (Fe_{py}) is calculated from the measured CRS content of each sample.

Total carbon and total inorganic carbon (TIC) contents were measured via IR spectroscopy of CO_2 using a CS-MAT 5500 carbon–sulphur analyzer. Sediment powder was combusted to CO_2 at 1350 °C for total carbon analysis. HCl was added to liberate CO_2 for total inorganic carbon contents. Total organic carbon (TOC) was calculated as the difference between total carbon and total inorganic carbon in the sediment. The reproducibility of the TOC analysis was typically better than ±2%.

For the analysis of $\delta^{13}C$ values, CO_2 was released from sediments using off-line phosphoric acid reaction method[86] with phosphoric acid of a nominal concentration of 103%[87] at 50 °C for 24 h and subsequent cryogenic distillation. Carbon isotope measurements were carried out with a Thermo-Finnigan DeltaPlus mass spectrometer at Institut für Geologie und Paläontologie, Westfälische Wilhelms-Universität Münster. Stable isotope results are expressed relative to the V-PDB standard. The carbon isotope measurements were calibrated with a carbonate standard ($\delta^{13}C = 1.46‰$). The analytical accuracy was better than ±0.1‰ for $\delta^{13}C$ values.

Powdered samples were digested with a mixture of concentrated HNO_3, HF, and $HClO_4$ acids. The solution was evaporated on a hotplate to near dryness and then re-dissolved in 100 ml 7 M HCl. The final solution was diluted in 2% HNO_3 solution and analysed with an Agilent 5110 inductively coupled plasma–atomic emission spectrometer (ICP-AES) for Al, Ti, K and P concentrations and analysed with an Agilent 7700 inductively coupled plasma mass spectrometer (ICP-MS) for Zr and Mo concentrations at the ALS Laboratory, Guangzhou. Analytical performance was monitored by repeatedly analysing certified reference materials (MRGeo08 and GBM908-10). Analytical precision was typically better than 7% for Zr, Ti, K, Ba, Mo and P, and better than 6% for Al.

Data availability

Supplementary figures and all relevant geochemistry datasets are available in the Supplementary Info file. Geochemistry datasets are available at Pangaea data publisher, titled as "Sample depth, magnetic susceptibility, elemental and sulphur isotope geochemistry for bulk sediments from core RKB 5260 in Lake Pannon".

References

1. Bastviken, D., Cole, J., Pace, M. & Tranvik, L. Methane emissions from lakes: dependence of lake characteristics, two regional assessments, and a global estimate. *Global Biogeochem. Cycles* **18**, GB4009 (2004).
2. Egger, M. et al. Iron-mediated anaerobic oxidation of methane in brackish coastal sediments. *Environ. Sci. Technol.* **49**, 277–283 (2015).
3. Dean, J. F. et al. Methane feedbacks to the global climate system in a warmer world. *Rev. Geophys.* **56**, 207–250 (2018).
4. Boetius, A. et al. A marine microbial consortium apparently mediating anaerobic oxidation of methane. *Nature* **407**, 623–626 (2000).
5. Holmer, M. & Storkholm, P. Sulphate reduction and sulphur cycling in lake sediments: a review. *Freshwat. Biol* **46**, 431–451 (2001).
6. Hinrichs, K.-U. & Boetius, A. The anaerobic oxidation of methane: new insights in microbial ecology and biogeochemistry. In *Ocean Margin Systems* (eds Wefer, G. et al.) 457–477 (Springer Berlin Heidelberg, 2002).
7. Sivan, O. et al. Geochemical evidence for iron-mediated anaerobic oxidation of methane. *Limnol. Oceanogr.* **56**, 1536–1544 (2011).
8. Crowe, S. A. et al. The methane cycle in ferruginous Lake Matano. *Geobiology* **9**, 61–78 (2011).
9. Segarra, K. E. A., Comerford, C., Slaughter, J. & Joye, S. B. Impact of electron acceptor availability on the anaerobic oxidation of methane in coastal freshwater and brackish wetland sediments. *Geochim. Cosmochim. Acta* **115**, 15–30 (2013).
10. Beal, E. J., Claire, M. W. & House, C. H. High rates of anaerobic methanotrophy at low sulfate concentrations with implications for past and present methane levels. *Geobiology* **9**, 131–139 (2011).
11. Segarra, K. E. A. et al. High rates of anaerobic methane oxidation in freshwater wetlands reduce potential atmospheric methane emissions. *Nat. Commun.* **6**, 7477 (2015).
12. Weston, N. B., Vile, M. A., Neubauer, S. C. & Velinsky, D. J. Accelerated microbial organic matter mineralization following salt-water intrusion into tidal freshwater marsh soils. *Biogeochemistry* **102**, 135–151 (2011).
13. Herbert, E. R. et al. A global perspective on wetland salinization: ecological consequences of a growing threat to freshwater wetlands. *Ecosphere* **6**, 1–43 (2015).
14. Bristow, T. F. & Grotzinger, J. P. Sulfate availability and the geological record of cold-seep deposits. *Geology* **41**, 811–814 (2013).
15. Sun, F. N. et al. Sustained and intensified lacustrine methane cycling during Early Permian climate warming. *Nat. Commun.* **13**, 4856 (2022).
16. Müller, P., Geary, D. H. & Magyar, I. The endemic molluscs of the Late Miocene Lake Pannon: their origin, evolution, and family-level taxonomy. *Lethaia* **32**, 47–60 (1999).
17. Neubauer, T. A., Harzhauser, M., Mandic, O., Kroh, A. & Georgopoulou, E. Evolution, turnovers and spatial variation of the gastropod fauna of the late Miocene biodiversity hotspot Lake Pannon. *Palaeogeogr. Palaeoclimatol. Palaeoecol.* **442**, 84–95 (2016).
18. Magyar, I., Geary, D. H. & Muller, P. Paleogeographic evolution of the Late Miocene Lake Pannon in Central Europe. *Palaeogeogr. Palaeoclimatol. Palaeoecol.* **147**, 151–167 (1999).
19. Magyar, I. Chronostratigraphy of clinothem-filled non-marine basins: dating the Pannonian stage. *Global Planet. Change* **205**, 103609 (2021).

20. Mátyás, J., Burns, S. J., Müller, P. & Magyar, I. What can stable isotopes say about salinity? An example from the late Miocene Pannonian lake. *Palaios* 11, 31–39 (1996).

21. Harzhauser, M., Latal, C. & Piller, W. E. The stable isotope archive of Lake Pannon as a mirror of Late Miocene climate change. *Palaeogeogr. Palaeoclimatol. Palaeoecol.* 249, 335–350 (2007).

22. Harzhauser, M., Piller, W. E. & Latal, C. Geodynamic impact on the stable isotope signatures in a shallow epicontinental sea. *Terra Nova* 19, 324–330 (2007).

23. Peckmann, J. et al. Methane-derived carbonates and authigenic pyrite from the northwestern Black Sea. *Mar. Geol.* 177, 129–150 (2001).

24. Lin, Z. Y. et al. How sulfate-driven anaerobic oxidation of methane affects the sulfur isotopic composition of pyrite: a SIMS study from the South China Sea. *Chem. Geol.* 440, 26–41 (2016).

25. Lin, Z. Y. et al. Effects of sulfate reduction processes on the trace element geochemistry of sedimentary pyrite in modern seep environments. *Geochim. Cosmochim. Acta* 333, 75–94 (2022).

26. Harzhauser, M. et al. The Sarmatian/Pannonian boundary at the western margin of the Vienna Basin (City of Vienna, Austria). *Austrian J. Earth Sci* 111, 1–26 (2018).

27. Harzhauser, M., Kranner, M., Mandic, O., Ćorić, S. & Siedl, W. High resolution Late Miocene sediment accommodation rates and subsidence history in the Austrian part of the Vienna Basin. *Mar. Pet. Geol.* 145, 105872 (2022).

28. Cziczer, I. et al. Life in the sublittoral zone of long-lived Lake Pannon: paleontological analysis of the Upper Miocene Szák Formation, Hungary. *Int. J. Earth Sci.* 98, 1741–1766 (2009).

29. Harzhauser, M. et al. Explosive demographic expansion by dreissenid bivalves as a possible result of astronomical forcing. *Biogeosciences* 10, 8423–8431 (2013).

30. Kern, A. K., Harzhauser, M., Piller, W. E., Mandic, O. & Soliman, A. Strong evidence for the influence of solar cycles on a Late Miocene lake system revealed by biotic and abiotic proxies. *Palaeogeogr. Palaeoclimatol. Palaeoecol.* 329, 124–136 (2012).

31. Kern, A. K., Harzhauser, M., Soliman, A., Piller, W. E. & Mandic, O. High-resolution analysis of upper Miocene lake deposits: evidence for the influence of Gleissberg-band solar forcing. *Palaeogeogr. Palaeoclimatol. Palaeoecol.* 370, 167–183 (2013).

32. Harzhauser, M. et al. Miocene lithostratigraphy of the northern and central Vienna Basin (Austria). *Austrian J. Earth Sci* 113, 169–199 (2020).

33. Siedl, W. et al. Revised Badenian (middle Miocene) depositional systems of the Austrian Vienna Basin based on a new sequence stratigraphic framework. *Austrian J. Earth Sci* 113, 87–110 (2020).

34. Pike, C. R., Roberts, A. P. & Verosub, K. L. Characterizing interactions in fine magnetic particle systems using first order reversal curves. *J. Appl. Phys.* 85, 6660–6667 (1999).

35. Roberts, A. P., Chang, L. A., Rowan, C. J., Horng, C. S. & Florindo, F. Magnetic properties of sedimentary greigite (Fe₃S₄): an update. *Rev. Geophys.* 49, RG1002 (2011).

36. Roberts, A. P. et al. Signatures of reductive magnetic mineral diagenesis from unmixing of first-order reversal curves. *J. Geophys. Res.-Solid Earth* 123, 4500–4522 (2018).

37. Jørgensen, B. B. Mineralization of organic matter in the sea bed—the role of sulphate reduction. *Nature* 296, 643–645 (1982).

38. Taylor, K. G. & Macquaker, J. H. S. Iron minerals in marine sediments record chemical environments. *Elements* 7, 113–118 (2011).

39. Rickard, D. *Framboids* (Oxford University Press, 2021).

40. Rickard, D. T. Kinetics and mechanism of pyrite formation at low temperatures. *Am. J. Sci.* 275, 636–652 (1975).

41. Rickard, D. & Luther, G. W. Kinetics of pyrite formation by the H₂S oxidation of iron (II) monosulfide in aqueous solutions between 25 and 125 °C: the mechanism. *Geochim. Cosmochim. Acta* 61, 135–147 (1997).

42. Hellige, K., Pollok, K., Larese-Casanova, P., Behrends, T. & Peiffer, S. Pathways of ferrous iron mineral formation upon sulfidation of lepidocrocite surfaces. *Geochim. Cosmochim. Acta* 81, 69–81 (2012).

43. Poulton, S. W. & Canfield, D. E. Ferruginous conditions: a dominant feature of the ocean through Earth's history. *Elements* 7, 107–112 (2011).

44. Harzhauser, M. et al. Environmental shifts in and around Lake Pannon during the Tortonian Thermal Maximum based on a multi-proxy record from the Vienna Basin (Austria, Late Miocene, Tortonian). *Palaeogeogr. Palaeoclimatol. Palaeoecol.* 610, 111332 (2023).

45. Lin, Z. Y. et al. Multiple sulfur isotope constraints on sulfate-driven anaerobic oxidation of methane: evidence from authigenic pyrite in seepage areas of the South China Sea. *Geochim. Cosmochim. Acta* 211, 153–173 (2017).

46. Liu, J. R. et al. Multiple sulfur isotopes discriminate organoclastic and methane-based sulfate reduction by sub-seafloor pyrite formation. *Geochim. Cosmochim. Acta* 316, 309–330 (2022).

47. Zhang, M. et al. Morphology and formation mechanism of pyrite induced by the anaerobic oxidation of methane from the continental slope of the NE South China Sea. *J. Asian Earth Sci.* 92, 293–301 (2014).

48. Canfield, D. E. Isotope fractionation by natural populations of sulfate-reducing bacteria. *Geochim. Cosmochim. Acta* 65, 1117–1124 (2001).

49. Lin, Z. Y. et al. Multiple sulfur isotopic evidence for the origin of elemental sulfur in an iron-dominated gas hydrate-bearing sedimentary environment. *Mar. Geol.* 403, 271–284 (2018).

50. Jørgensen, B. B., Böttcher, M. E., Luschen, H., Neretin, L. N. & Volkov, I. I. Anaerobic methane oxidation and a deep H₂S sink generate isotopically heavy sulfides in Black Sea sediments. *Geochim. Cosmochim. Acta* 68, 2095–2118 (2004).

51. Borowski, W. S., Rodriguez, N. M., Paull, C. K. & Ussler, W. Are ³⁴S-enriched authigenic sulfide minerals a proxy for elevated methane flux and gas hydrates in the geologic record? *Mar. Pet. Geol.* 43, 381–395 (2013).

52. Tostevin, R. et al. Multiple sulfur isotope constraints on the modern sulfur cycle. *Earth Planet. Sci. Lett.* 396, 14–21 (2014).

53. Crémière, A., Pellerin, A., Wing, B. A. & Lepland, A. Multiple sulfur isotopes in methane seep carbonates track unsteady sulfur cycling during anaerobic methane oxidation. *Earth Planet. Sci. Lett.* 531, 115994 (2020).

54. Peckmann, J. & Thiel, V. Carbon cycling at ancient methane–seeps. *Chem. Geol.* 205, 443–467 (2004).

55. Peketi, A. et al. Coupled C-S-Fe geochemistry in a rapidly accumulating marine sedimentary system: Diagenetic and depositional implications. *Geochem. Geophys. Geosyst.* 16, 2865–2883 (2015).

56. Hu, Y. et al. The impact of diffusive transport of methane on pore-water and sediment geochemistry constrained by authigenic enrichments of carbon, sulfur, and trace elements: a case study from the Shenhu area of the South China Sea. *Chem. Geol.* 553, 119805 (2020).

57. Peketi, A. et al. Tracing the paleo sulfate-methane transition zones and H₂S seepage events in marine sediments: an application of C-S-Mo systematics. *Geochem. Geophys. Geosyst.* 13, 1–11 (2012).

58. Borowski, W. S., Paull, C. K. & Ussler, W. Carbon cycling within the upper methanogenic zone of continental rise sediments; An example from the methane-rich sediments overlying the Blake Ridge gas hydrate deposits. *Mar. Chem.* 57, 299–311 (1997).

59. Riedinger, N. et al. An inorganic geochemical argument for coupled anaerobic oxidation of methane and iron reduction in marine sediments. *Geobiology* 12, 172–181 (2014).

60. Hilton, J. Greigite and the magnetic properties of sediments. *Limnol. Oceanogr.* 35, 509–520 (1990).

61. Roberts, A. P., Reynolds, R. L., Verosub, K. L. & Adam, D. P. Environmental magnetic implications of greigite (Fe₃S₄) formation in a 3 m.y. lake sediment record from Butte Valley, northern California. *Geophys. Res. Lett.* 23, 2859–2862 (1996).

62. Snowball, I. & Thompson, R. The occurrence of Greigite in sediments from Loch Lomond. *J. Quat. Sci.* 3, 121–125 (1988).

63. Fu, Y. Z., von Dobeneck, T., Franke, C., Heslop, D. & Kasten, S. Rock magnetic identification and geochemical process models of greigite formation in Quaternary marine sediments from the Gulf of Mexico (IODP Hole U1319A). *Earth Planet. Sci. Lett.* 275, 233–245 (2008).

64. Larrasoaña, J. C. et al. Diagenetic formation of greigite and pyrrhotite in gas hydrate marine sedimentary systems. *Earth Planet. Sci. Lett.* 261, 350–366 (2007).

65. Neretin, L. N. et al. Pyritization processes and greigite formation in the advancing sulfidization front in the Upper Pleistocene sediments of the Black Sea. *Geochim. Cosmochim. Acta* 68, 2081–2093 (2004).

66. Roberts, A. P. Magnetic mineral diagenesis. *Earth-Sci. Rev.* 151, 1–47 (2015).

67. Gong, S. et al. Multiple sulfur isotope systematics of pyrite for tracing sulfate-driven anaerobic oxidation of methane. *Earth Planet. Sci. Lett.* 597, 117827 (2022).

68. Lin, Z. Y. et al. Molybdenum isotope composition of seep carbonates—constraints on sediment biogeochemistry in seepage environments. *Geochim. Cosmochim. Acta* 307, 56–71 (2021).

69. Chen, F. et al. Evidence of intense methane seepages from molybdenum enrichments in gas hydrate-bearing sediments of the northern South China Sea. *Chem. Geol.* 443, 173–181 (2016).

70. Dickens, G. R. Sulfate profiles and barium fronts in sediment on the Blake Ridge: present and past methane fluxes through a large gas hydrate reservoir. *Geochim. Cosmochim. Acta* 65, 529–543 (2001).

71. Teichert, B. M. A. et al. U/Th systematics and ages of authigenic carbonates from Hydrate Ridge, Cascadia Margin: recorders of fluid flow variations. *Geochim. Cosmochim. Acta* 67, 3845–3857 (2003).

72. Riedinger, N. et al. Diagenetic alteration of magnetic signals by anaerobic oxidation of methane related to a change in sedimentation rate. *Geochim. Cosmochim. Acta* 69, 4117–4126 (2005).

73. Henkel, S., Kasten, S., Poulton, S. W. & Staubwasser, M. Determination of the stable iron isotopic composition of sequentially leached iron phases in marine sediments. *Chem. Geol.* 421, 93–102 (2016).

74. Laufer, K., Michaud, A. B., Roy, H. & Jorgensen, B. B. Reactivity of iron minerals in the seabed toward microbial reduction – a comparison of different extraction techniques. *Geomicrobiol. J.* 37, 170–189 (2020).

75. Poulton, S. W. & Canfield, D. E. Development of a sequential extraction procedure for iron: implications for iron partitioning in continentally derived particulates. *Chem. Geol.* **214**, 209–221 (2005).

76. Lin, Z. Y. et al. A novel authigenic magnetite source for sedimentary magnetization. *Geology* **49**, 360–365 (2021).

77. Balci, N., Shanks, I. I. I. W. C., Mayer, B. & Mandernack, K. W. Oxygen and sulfur isotope systematics of sulfate produced by bacterial and abiotic oxidation of pyrite. *Geochim. Cosmochim. Acta* **71**, 3796–3811 (2007).

78. Canfield, D. E., Raiswell, R., Westrich, J. T., Reaves, C. M. & Berner, R. A. The use of chromium reduction in the analysis of reduced inorganic sulfur in sediments and shales. *Chem. Geol.* **54**, 149–155 (1986).

79. Rice, C. A., Tuttle, M. L. & Reynolds, R. L. The analysis of forms of sulfur in ancient sediments and sedimentary rocks: comments and cautions. *Chem. Geol.* **107**, 83–95 (1993).

80. Brand, W. A., Coplen, T. B., Vogl, J., Rosner, M. & Prohaska, T. Assessment of international reference materials for isotope-ratio analysis (IUPAC Technical Report). *Pure Appl. Chem.* **86**, 425–467 (2014).

81. Ono, S., Wing, B., Johnston, D., Farquhar, J. & Rumble, D. Mass-dependent fractionation of quadruple stable sulfur isotope system as a new tracer of sulfur biogeochemical cycles. *Geochim. Cosmochim. Acta* **70**, 2238–2252 (2006).

82. Farquhar, J., Bao, H. M. & Thiemens, M. Atmospheric influence of Earth's earliest sulfur cycle. *Science* **289**, 756–758 (2000).

83. Li, R. C., Xia, X. P., Yang, S. H., Chen, H. Y. & Yang, Q. Off-mount calibration and one new potential pyrrhotite reference material for sulfur isotope measurement by secondary ion mass spectrometry. *Geostand. Geoanal. Res.* **43**, 177–187 (2019).

84. Ushikubo, T. et al. Development of in situ sulfur four-isotope analysis with multiple Faraday cup detectors by SIMS and application to pyrite grains in a Paleoproterozoic glaciogenic sandstone. *Chem. Geol.* **383**, 86–99 (2014).

85. Gilbert, S. E. et al. Optimisation of laser parameters for the analysis of sulphur isotopes in sulphide minerals by laser ablation ICP-MS. *J. Anal. At. Spectrom.* **29**, 1042–1051 (2014).

86. McCrea, J. M. On the isotopic chemistry of carbonates and a paleotemperture scale. *The J. Chem. Phys.* **18**, 849–857 (1950).

87. Wachter, E. A. & Hayes, J. M. Exchange of oxygen isotopes and carbon isotopes in carbon dioxide-phosphoric acid systems. *Chem. Geol.* **52**, 365–374 (1985).

88. Heslop, D. et al. An automatic model selection-based machine learning framework to estimate FORC distributions. *J. Geophys. Res. Solid Earth* **125**, e2020JB020418 (2020).

89. Egli, R. VARIFORC: an optimized protocol for calculating non-regular first-order reversal curve (FORC) diagrams. *Global Planet. Change* **110**, 302–320 (2013).

Author contributions
Z.L., H.S. and M.H. designed the study; Z.L., H.S., Y.L. and T.C. carried out the laboratory work; Z.L. wrote the manuscript and H.S., A.R., X.S. and J.P. contributed to data interpretation and manuscript refinement.

Competing interests
The authors declare no competing interests.

Additional information
Supplementary information The online version contains supplementary material available at https://doi.org/10.1038/s43247-023-00879-2.

Correspondence and requests for materials should be addressed to Zhiyong Lin.

Peer review information *Communications Earth & Environment* thanks Guillaume Paris, Jakob Zopfi, and the other, anonymous, reviewer(s) for their contribution to the peer review of this work. Primary Handling Editors: Mojtaba Fakhraee and Joe Aslin. A peer review file is available.

Reprints and permission information is available at http://www.nature.com/reprints

Publisher's note Springer Nature remains neutral with regard to jurisdictional claims in published maps and institutional affiliations.